Dynamics of competitive binding and separation of monoclonal antibody monomer-dimer mixtures in ceramic hydroxyapatite columns

Yiran Wang, Giorgio Carta*

Department of Chemical Engineering, University of Virginia, Charlottesville, VA, USA

A R T I C L E   I N F O

A B S T R A C T

This work examines the separation dynamics of monoclonal antibody monomer/dimer mixtures by frontal analysis using ceramic hydroxyapatite CHT Type I and Type II columns. The binding capacity and selectivity are dependent on the CHT type and salt concentration. While the rate of protein adsorption on CHT Type I is slow and controlled largely by pore diffusion resulting in relatively poor separation, adsorption on CHT Type II is much faster and better separation is obtained than with Type I. However, comparison with predictions based on pore diffusion alone, reveals the presence of additional resistances associated with adsorption and displacement kinetics. A spreading kinetics model assuming multiple binding configurations coupled with pore diffusion was developed to describe these effects and found to be in quantitative agreement with the frontal analysis results and able to predict the separation achieved for conditions outside the range of the experiments. To help validate the assumed mechanism, isocratic elution experiments were also conducted at low protein loads. The chromatograms could be described by the solution of the spreading model coupled with pore diffusion in the linear region of the isotherm with parameters determined from the analytical expressions for the peak moments. This confirms that there is an increasing tendency to spread with slower kinetics as the salt concentration is decreased and binding strength is increased.

© 2019 Elsevier B.V. All rights reserved.

1. Introduction

As a chromatographic medium, ceramic hydroxyapatite (CHT) consists of hydroxyapatite (HAP) nanocrystals with bulk formula $Ca_5(PO_4)_3OH$ that are spray dried and then sintered at high temperature to obtain nearly spherical macroporous beads with high mechanical stability. The sintering temperature is known to affect the crystal morphology and, thus, pore size as well as the available surface area [1,2]. Different types of CHT are commercially available and are usually classified according to these properties. For example, CHT Type I and CHT Type II, available from Bio-Rad Laboratories (Hercules, CA, USA), differ principally in pore radius and porosity. As shown in our prior work, effective pore radii and surface areas are around 30 and 49 nm and 33 and 20 m²/mL for Type I and Type II, respectively [3]. These materials are commercially available in different particle sizes (e.g. 40–80 μm), which are suitable for large scale, low-pressure chromatographic separations.

For both CHT Type I and CHT Type II, the HAP crystal surface is believed to comprise negatively-charged phosphate groups (referred to as P-sites) as well as positively-charged calcium ions

(C-sites) [4–7]. As a result, proteins interact with the surface with a potentially complex, multimodal mechanism dependent on electrostatic interactions with the P-sites and on calcium affinity mechanisms on the C-sites. In practice, however, around neutral pH and at modest ionic strengths in solution, cationic proteins, such as many monoclonal antibodies, bind to the HAP surface primarily as a result of a cation-exchange mechanism on the P-sites, while acidic proteins and nucleic acids bind primarily as a result of complexation of carboxyl and phosphoryl groups on the C-sites. Because of the different binding mechanisms, cationic proteins are typically desorbed at high salt concentrations, while acidic proteins will often require competitive displacers to break the calcium-protein interaction. Obviously, it is possible for some proteins to interact simultaneously via both mechanisms, resulting in unique selectivities. Many practical applications of CHT as a chromatographic medium have been developed over the years based on these unique selectivities along with the absence of hydrophobic interaction, including the purification of DNA, enzymes, virus-like particles, and immunoglobulins [8–13]. Industrially, one of the major applications of HAP is the removal of aggregates in monoclonal antibody (mAb) purification [14–16].

Because of the relatively large size of the molecules involved and the relatively large size of the CHT particles, mass transfer

* Corresponding author.
  E-mail address: gc@virginia.edu (G. Carta).

resistance are significant when these materials are used for protein separations. Yet, despite the popularity of CHT in practical applications, few studies have been published addressing protein adsorption kinetics and column dynamics, especially, for multicomponent systems at high loadings. An exception is our recent work aimed at characterizing the competitive binding of monoclonal antibody monomer-dimer mixtures [3]. In this work, we measured monomer and dimer mass transfer rates under non-binding conditions, determined adsorption isotherms for single component and mixture adsorption over a range of salt concentrations, and observed one and two-component adsorption kinetics using confocal laser scanning microscopy (CLSM). We observed that both monomer and dimer adsorption kinetics are affected by intraparticle diffusion for both Type I and Type II. However, the effect is much more pronounced for the dimer compared to the monomer, due to the larger size of the former, and also for Type I compared to Type II, because of the smaller pore size of the former. One of the key results of our prior work was that, despite the presence of significant mass transfer limitations, displacement of the monomer by the dimer still occurs over relatively short time scales during mixture adsorption resulting in selective binding of the dimer relative to the monomer. This result suggests that separation of antibody monomer-dimer mixtures could be carried by frontal analysis (or frontal loading) in CHT columns at reasonable flow rates.

Interest in this mode of operation, formally defined by Tiselius in 1940s, has increased in recent years for protein separations. This interest stems in part from the fact that frontal analysis generally affords a higher utilization of the binding capacity compared to gradient elution, and in part because the separation can be conducted under isocratic conditions, thereby simplifying operations. In this mode of operation, a binary mixture is continuously loaded to the column resulting in two adsorption fronts – a fast moving front, corresponding to the more weakly bound component, and a more slowly moving front corresponding to breakthrough of the more strongly bound component. Under ideal conditions, the weakly bound component is recovered in the column effluent between the first and the second front, while the more strongly bound component is held in the column and is recovered by elution together with any of the weakly bound components. If more than two components are present with greater binding strength, each of the more strongly bound species accumulates in the column and is removed during the elution step. Application of frontal analysis to protein purification has been demonstrated by several authors using either cation exchange resins for the separation of antibody charge variants [17] and antibody monomer-dimer mixtures [18] or anion exchange resins and adsorptive membranes for the separation of albumin monomer and aggregates [19,20]. Although described with different terms such as "overload chromatography" [21,22] and "flow-through chromatography" [23], frontal analysis has also been used to separate antibodies from aggregates and other impurities using either resins or adsorptive membranes.

The objectives of this work are twofold. The first is to establish experimentally the feasibility of separating antibody monomer-dimer mixtures by frontal analysis at reasonable residence times. The second is to develop a mechanistic model to predict the separation. We expect the column dynamics to be influenced by mass transfer and, thus, dependent on residence time. However, additional factors related to the kinetics of displacement of the monomer by the dimer could also play a role. Thus, while diffusional mass transfer kinetics is the starting point, we consider models that also account for potential kinetics limitations affecting the exchange of monomer for dimer molecules on the adsorbent surface. Such a model can then be used to predict separation as a function of residence time, protein concentration, and the monomer/dimer ratio in the feed. As in our prior work [3], we consider both CHT Type I and Type II, which will help understand the influence of the physical properties of these materials on the chromatography. Experimental measurements and modeling are used synergistically to understand the controlling factors in both cases.

2. Experimental

2.1. Materials

The CHT samples used in this work were the same as those used previously [3] and were obtained from Bio-Rad Laboratories (Hercules, CA, USA). Particle diameters were determined from photomicrographs and volume average values were 41.3 and 39.9 μm for Type I and II, respectively. Pore radii, determined by inverse size exclusion chromatography, were 30 ± 4 and 49 ± 2 nm for Type I and Type II, respectively, with corresponding intraparticle porosities of 0.73 and 0.70. Intraparticle porosities accessible by antibody monomer and dimer molecules under non-binding conditions, ε_p', were 0.52 and 0.47, respectively, for Type I and 0.61 and 0.58, respectively, for Type II.

The monoclonal antibody samples used in this work were derived from a mixture containing about 68% monomer and 32% dimer provided by AstraZeneca (Gaithersburg, MD, USA), the same as that used in refs. [24,3]. As discussed previously, both monomer and dimer are stable showing no evidence of further aggregation or disaggregation even after 24 h in solution at room temperature. Purified monomer and purified dimer samples were isolated from this mixture using a preparative size exclusion chromatography column (Superdex 200 Increase 10/300 GL, from GE Healthcare, Pittsburg, PA, USA) and concentrated using a 30 kDa MWCO Amicon Ultra-15 centrifugal filter unit (Millipore, Billerica, MA,USA) as described in ref. [24]. The purity of isolated monomer and dimer samples were both well over 95%.

All of the protein samples were buffer exchanged into different running buffer using a HiPrep 26/10 desalting column (GE Healthcare, Pittsburgh, PA, USA). As reported by Reck et al. [24], the pI is 8.6 for both monomer and dimer, while the corresponding free solution diffusivities, D_0, and hydrodynamic radii are 3.9×10^{-7} and 2.8×10^{-7} cm^2/s and 5.5 and 7.2 nm, respectively. All other chemicals used in buffer preparations were purchased from Thermo Fisher Scientific (Pittsburgh, PA, USA) and MilliporeSigma (St. Louis, MO, USA).

2.2. Batch adsorption equilibrium and kinetics measurements

Some additional adsorption equilibrium and kinetics measurements were conducted to supplement our previous data [3] by extending the number of experimental measurements and the range of salt concentration. Adsorption equilibrium measurements were obtained by mixing CHT beads with solutions containing different protein concentrations for a period of 24 h and measuring the residual concentrations in solution by UV and by analytical size exclusion chromatography as described previously [3]. The amount of each protein adsorbed, q_i, was obtained by material balance and normalized by the volume of CHT particles. Additional co-adsorption kinetics measurements were also conducted by confocal laser scanning microscopy (CLSM) for a monomer-dimer mixture in 10 mM Na$_2$HPO$_4$ with additional 50 mM NaCl at pH 7. These co-adsorption experiments were conducted using the monomer conjugated to Rhodamine red and the dimer conjugated to Rhodamine green as fluorescent tracers and used to determine the effective pore diffusivity, D_e, of monomer and dimer in both CHT Type I and Type II as described previously [3]. Images from these measurements and the procedure used to determine D_e are provided in the Supplementary Materials.

2.3. Column experiments

Frontal analysis experiments were conducted using 5 mm diameter × 50 mm long Tricorn 5/50 columns from GE Healthcare packed with CHT Type I or Type II. Following the CHT supplier instructions, both columns were flow-packed in a 10 mM Na$_2$HPO$_4$ buffer at pH 7.0 containing 1 M NaCl at a flow rate of 2 mL/min while mechanically tapping the column sharply until the bed height stabilized. Actual bed heights were 2.3 and 2.5 cm, for CHT Type I and Type II, respectively, with corresponding bed volumes of 0.45 and 0.49 mL. Although these columns are short in order to conserve materials, we operated them at flow rates sufficiently low to obtain reasonable residence times (see below). Since we expect mass transfer effects to be dominant, residence time, rather than bed height alone, is the relevant criterion for the choice of experimental conditions [25,26]. The packing quality was determined from NaCl pulse injections, which gave reduced HETP ($h = $ HETP$/d_p$, where d_p is the average particle diameter) of 8.6 and 9.0, and asymmetry factors of 1.68 and 1.52 for Type I and II, respectively. Values of the extraparticle porosity, ε, in these columns were 0.33 and 0.29 for Type I and Type II, respectively, determined from the elution volume of pulse injections of 600 kDa polyethylene glycol. For the frontal analysis runs the load flow rate was varied between 0.08 and 0.2 mL/min corresponding to residence times between 2.5 and 5.6 min. The total protein concentration in the feed mixture was 2.0 ± 0.2 mg/mL with dimer content varying between 17 and 32%. The effluent from the column was collected in 1 mL increments into 2 mL tubes (Becton Dickinson, Lincoln Park, NJ, USA) using a Model F9-R fraction collector from GE Healthcare (Pittsburgh, PA, USA). Monomer and dimer concentrations were then determined using analytical SEC with a Waters Acquity BEH SEC 200 column (4.6 × 150 mm, 1.7 particle size) using a Waters Acquity H–Class UPLC system (Milford, MA, USA) as described in ref. [24]. Single component breakthrough curves were also obtained for the monomer with just UV detection of the effluent profile. Following each experiment, the columns were stripped with 500 mM Na$_2$HPO$_4$ at pH 7.0 and cleaned with 1 M NaOH.

Isocratic elution experiments were carried out with the isolated monomer and dimer samples at relatively high salt concentrations where binding is weak and follows a linear isotherm. For these experiments, CHT was packed into 10 mm diameter × 100 mm long Tricorn 10/100 columns (GE Healthcare) at 5 mL/min to a final bed volumes of 6.7 ± 0.1 mL, corresponding to bed heights of 8.5 ± 0.1 cm. The packing quality was again determined from NaCl pulse injections, which gave reduced HETP values of 3.9 and 2.5 and asymmetry factors of 1.2 and 1.1 for Type I and II, respectively. The extraparticle porosity in these columns was 0.29 and 0.30 for Type I and Type II, respectively. For the isocratic elution experiments, the isolated monomer and dimer samples were buffer-exchanged into the running buffer injected individually into the column in 100 μL volume and eluted at 1 mL/min. The columns were stripped with 500 mM Na$_2$HPO$_4$ and re-equilibrated in the running buffer after each chromatographic run.

3. Experimental results

3.1. Protein adsorption equilibrium

Fig. 1 shows the isotherm data for monomer and dimer as single components and as mixture in the concentration range of 0–8 mg/mL for the monomer and 0–3 mg/mL for the dimer in 10 mM Na$_2$HPO$_4$ buffers at pH 7 containing 0, 50, 80, and 160 mM NaCl The corresponding Na$^+$ concentrations were 20, 70, 100, and 180 mM. Additional viewing angles are provided in Figure S.1 in the Supplementary Material.

As shown previously [3], the sodium ion concentration determines both monomer and dimer binding regardless of the specific phosphate concentration at these relatively high phosphate levels. Preferential binding of the dimer relative to the monomer is evident from Fig. 1 at each Na$^+$ concentration as seen from the steep drop of monomer binding, q_M, along the C_D axis, compared to the much shallower drop of dimer binding, q_D, along the C_M axis. The data set was fitted to the two-component Langmuir isotherm:

$$q_i = \frac{q_{m,i} K_i C_i}{1 + K_M C_M + K_D C_D} \tag{1}$$

with parameters $q_{m,i}$ and K_i regressed to the data individually at each Na$^+$ concentration. These parameters are summarized in Table 1 and calculated surfaces are shown in Fig. 1. Both the experimental results and the fitted parameters are in agreement with our previous measurements. Although, as seen in this table, the regression error of the fitted parameters K_M and K_D is large due to the steepness of the pure-component isotherms especially at low Na$^+$ concentrations, predictions of the mixture binding capacities based on Eq. (1) using the mean values of the regressed coefficients were fairly accurate giving an average absolute error of 6–12% for the monomer and 3–6% for the dimer on Type I and 10–19% for the monomer and 2–7% for the dimer on Type II.

In prior work [24], we have shown that while double in molecular mass, the dimer is only about 30% larger than the monomer in terms of hydrodynamic radius, indicating that both monomer and dimer are in a globular form. Nevertheless, we have shown previously that, despite being relatively close in physical size, the effective binding charge of the dimer on a cation exchange resin was much higher than that of the monomer (14.8 vs. 10.2), which resulted in stronger binding of the dimer. We hypothesize that the mechanism leading to selectivity for the dimer is similar in CHT and that it is driven by the larger footprint of the dimer allowing stronger interactions with the phosphate groups on the hydroxyapatite crystals. As a result, it is likely that selective binding of the dimer and displacement of the monomer by the dimer results from a cation exchange mechanism where the species with the higher binding charge is preferred [3].

3.2. Separation by frontal analysis

Fig. 2 shows the binary breakthrough curves and the monomer purity obtained during frontal loading of monomer-dimer mixtures containing 32% dimer obtained at a residence time of 5.0 min with the CHT Type I column (top panels) and at a residence time of 5.6 min with the Type II column (bottom panels) in buffers containing either 20 mM Na$^+$ (left panels) or 70 mM Na$^+$ (right panels). Fig. 3 shows additional results for the CHT Type II column with a load buffer containing (a) 100 mM Na$^+$ and (b) 70 mM Na$^+$ as in Fig. 2d, but with a lower dimer content of 17% and a shorter residence time of 2.5 min. In each case, two-component breakthrough profiles calculated assuming local equilibrium conditions and no axial dispersion are also shown. These profiles were calculated according to the following equations [25,26]:

$$CV_I = \varepsilon + (1 - \varepsilon) \frac{q_M \left(C'_M, 0 \right)}{C'_M} \tag{2}$$

$$CV_{II} = \varepsilon + (1 - \varepsilon) \frac{q_M \left(C'_M, 0 \right) - q_M \left(C_M{}^F, C_D{}^F \right)}{C'_M - C_M{}^F}$$

$$= \varepsilon + (1 - \varepsilon) \frac{q_D \left(C_M^F, C_D{}^F \right)}{C_D{}^F} \tag{3}$$

where CV_I and CV_{II} are indicate the pure monomer breakthrough front and the monomer-dimer displacement front, respectively, both in column volume units, C'_M is the pure monomer plateau concentration, and C_M^F and C_D^F are the feed monomer and dimer
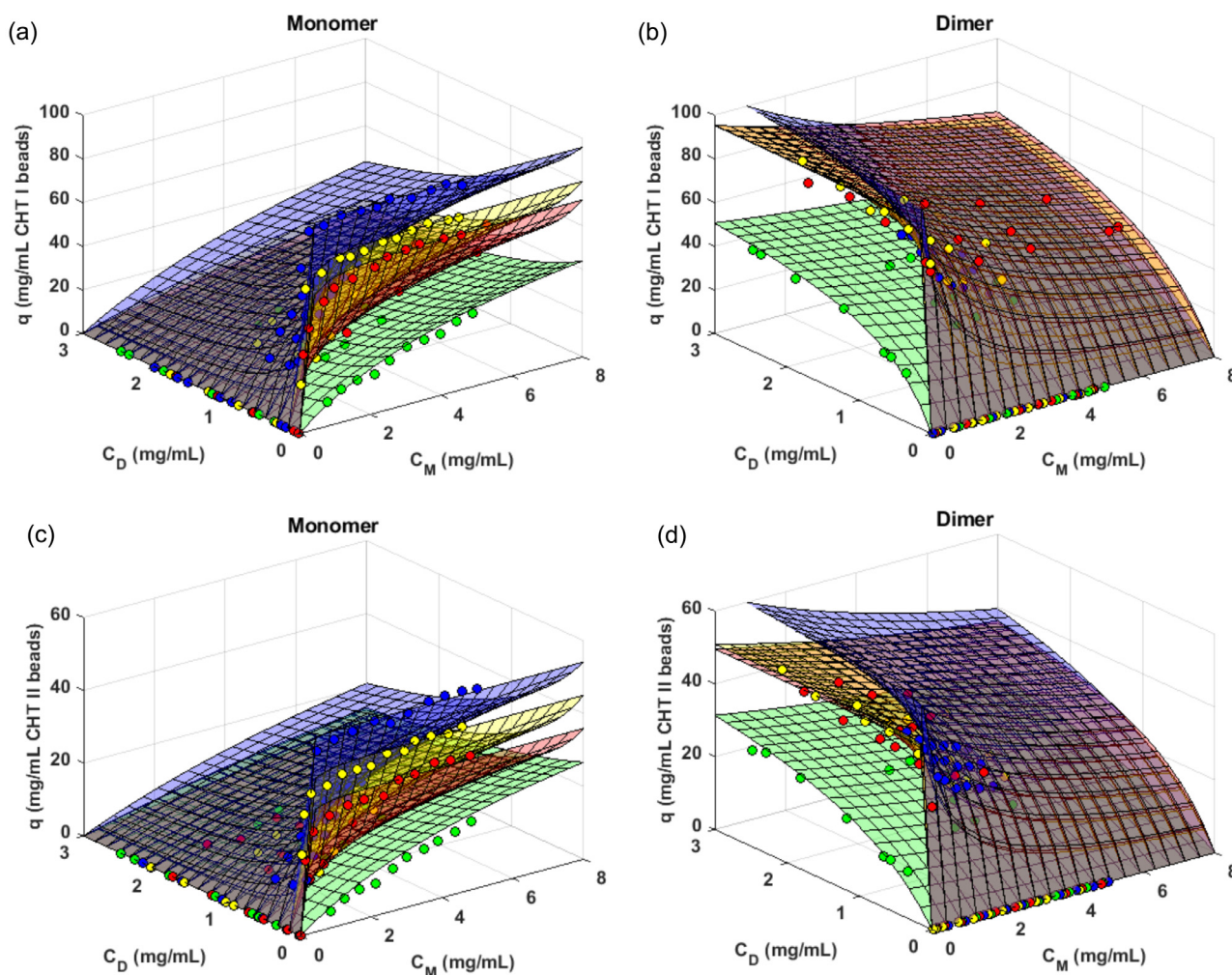
Fig. 1. Multi-component adsorption isotherms on CHT Type I (a, b) and CHT Type II (c, d) for the monomer (a, c) and for the dimer (b, d) in 10 mM Na$_2$HPO$_4$ buffers containing different NaCl concentrations at pH 7. The dots in blue, yellow, red and green represent 20, 70, 100 and 180 mM Na$^+$ concentrations, respectively. The surface lines are calculated with the two-component Langmuir isotherm model (Eq. (1)) using the best-fit parameters given in Table 1. (For interpretation of the references to color in this figure legend, the reader is referred to the web version of this article.)

Table 1
Langmuir isotherm parameters fitted to the data in Fig. 1 according to Eq. (1). $q_{m,i}$ values are in mg/mL of CHT bead volume and K_i values are in mL/mg.

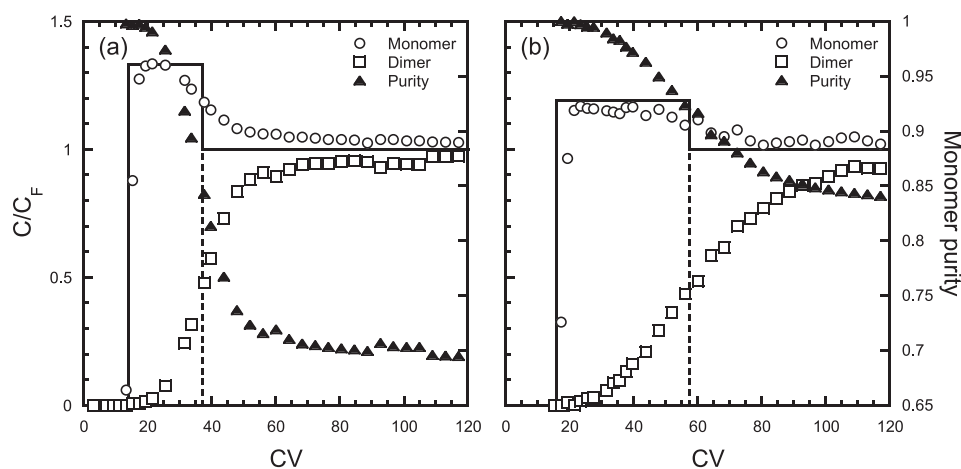| [Na$^+$] (mM)	CHT Type I				CHT Type II			
	$q_{m,M}$	K_M	$q_{m,D}$	K_D	$q_{m,M}$	K_M	$q_{m,D}$	K_D
20	96 ± 2	140 ± 55	110 ± 2	460 ± 180	52 ± 2	170 ± 260	64 ± 2	710 ± 120
70	81 ± 3	17 ± 4	96 ± 3	934 ± 25	45 ± 1	35 ± 9	51 ± 1	220 ± 59
100	73 ± 3	13 ± 4	96 ± 5	80 ± 26	36 ± 2	35 ± 17	50 ± 2	250 ± 110
180	70 ± 7	0.2 ± 0.0	64 ± 3	1.3 ± 0.2	47 ± 8	0.2 ± 0.0	47 ± 4	0.7 ± 0.1

concentrations, respectively. Binding capacities $q_M(C_M, C_D)$ and $q_D(C_M, C_D)$ are given by the two-component isotherms and are calculated for pure monomer at equilibrium with C'_M and for the monomer and dimer at equilibrium with the feed mixture using the isotherm parameter values in Table 1. As seen in these figures, the two-component breakthrough curves conform qualitatively with the local equilibrium predictions based on Eqs. (2) and (3) for both Type I and Type II. This qualitative agreement is indicated by (a) the overshoot of the monomer breakthrough curve above its feed concentration, which indicates displacement of the monomer by the dimer, and (b) the positions of the pure monomer breakthrough front and of the monomer-dimer displacement front relative to the solid and dashed lines in this figure that were calculated directly from the binding isotherms. The actual profiles are,

of course, broader than those predicted under ideal conditions, but the transitions and the qualitative trends are similar to those predicted by the equilibrium model.

Despite the qualitative agreement with the local equilibrium relationships, the experimental profiles and the corresponding monomer purity are strongly dependent on the CHT type, on the Na$^+$ concentration, and on the residence time. In all cases, while the pure monomer breakthrough profile remains very sharp, the displacement front is much broader than predicted under local equilibrium conditions. This discrepancy is especially pronounced for CHT Type I (Fig. 2a and b), at low Na$^+$ concentrations (Fig. 2a and c) and at low residence times (Fig. 3b). The monomer purity is also affected, of course. While, under ideal conditions, the monomer purity is predicted to be 100% between the pure
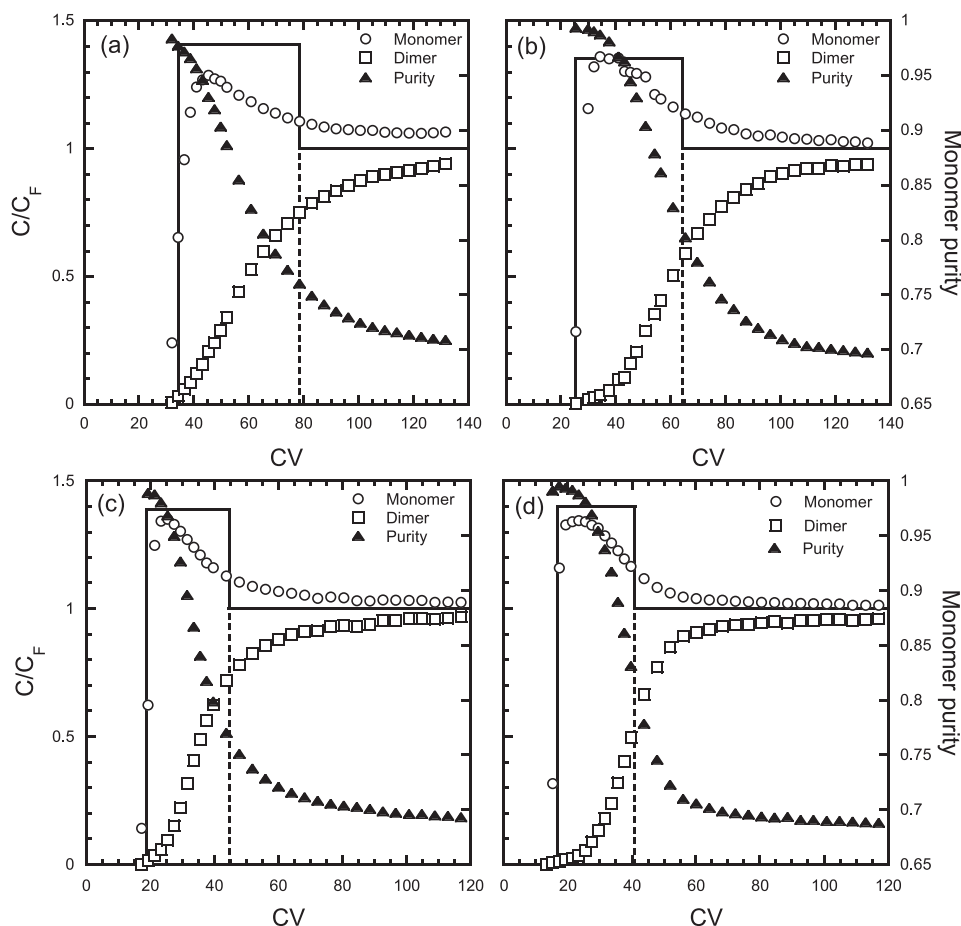
Fig. 2. Binary breakthrough curves of monomer-dimer mixtures containing approximately 30% dimer on CHT Type I (a, b) and CHT Type II (c, d) in 10 mM Na$_2$HPO$_4$ load buffers containing different NaCl concentrations at pH 7. (a, c) 20 mM Na$^+$, (b, d) 70 mM Na$^+$. The solid and dashed lines are model prediction based on Eqs. (2) and (3) using the parameters listed in Table 1. The residence time was 5.0 min in (a) and (b) and 5.6 min in (c) and (d).

Fig. 3. Binary breakthrough curves of monomer-dimer mixtures on CHT Type II containing approximately 30% dimer (a) and 17% dimer (b). The load buffers were 10 mM Na$_2$HPO$_4$ with different NaCl concentrations at pH 7 corresponding to 100 mM Na$^+$ (a) and 70 mM Na$^+$ (b). The solid and dashed lines are model predictions based Eqs. (2) and (3) using the parameters listed in Table 1. The residence time was 5.6 min in (a) and 2.5 min in (b).

monomer front and the displacement front, the data show values below this prediction.

From a practical viewpoint, selection of conditions that could be used to optimize monomer-dimer separations by frontal analysis with CHT could be done, in principle, just based on the experimental observations. For example, it is obvious that while CHT Type I has greater binding capacity than Type II leading to a greater separation between the pure monomer front and the mixture front, it also exhibits broader breakthrough profiles. As a result, at these relatively short residence times, much of the advantage of the greater binding capacity of Type I is lost. Operating at higher Na$^+$ concentrations (e.g. 70 mM Na$^+$ vs. 20 mM Na$^+$) also

reduces binding capacity and, thus, reduces the distance between the pure monomer front and the monomer-dimer displacement front, but also results in a sharper displacement front and, thus, better separation. This effect is especially evident for CHT Type II and can be seen comparing Fig. 2c and d, with 20 and 70 mM Na⁺, respectively. Going further up in Na⁺ concentration to, for example, 100 mM Na⁺, as seen in Fig. 3a, does result in a slightly sharper displacement front, but further reduces the binding capacity. As suggested by Figs. 2 and 3, the combination of binding capacity and sharpness of the displacement front will ultimately determine the separation performance defined, for example, in terms of pooled monomer purity and yield. The separation performance will vary depending on the CHT type and the Na⁺ concentration. The relationship between pooled monomer purity and yield and the protein load is evident qualitatively from Figs. 2 and 3 and is shown quantitatively in the Supplementary Materials (Figs. S.2). Both CHT type and Na⁺ concentration affect these relationships through their impact on binding capacity and band broadening. CHT Type I and lower Na⁺ result in greater loadability compared to CHT Type II and higher Na⁺, but also lower monomer recovery for a given pooled monomer purity or lower pooled monomer purity for a given monomer recovery.

A mechanistic model capable of describing the separation would help select conditions and reduce the extent of experimentation. For example, such a model could be used to find an optimum residence time that will provide a suitable compromise of capacity utilization, which is higher at lower flow rates, and process speed, which is faster at higher flow rates, or to predict the effects of varying the percentage of dimer in the feed mixture. Such a model can also help explain the relative importance of mass transfer and binding kinetics and help understand the root causes of the behaviors observed experimentally.

4. Model development

In order to successfully model frontal analysis, both mass transfer effects as well as any relevant kinetic resistance occurring during binding and displacement of one species by the other must be taken into account. Flow non-uniformity may also have to be considered to model actual large-scale columns. Our analysis is, however, limited to well-packed columns with nearly uniform velocity, such as those used in our laboratory experiments. For these conditions, the material balance equations are written as follows:

$$\varepsilon D_L \frac{\partial^2 C_i}{\partial x^2} = u \frac{\partial C_i}{\partial x} + \varepsilon \frac{\partial C_i}{\partial t} + (1 - \varepsilon) \frac{\partial \langle \hat{q}_i \rangle}{\partial t} \tag{4}$$

$$x = 0, C_i = C_i^F \tag{4a}$$

$$x = L, \quad \frac{\partial C_i}{\partial x} = 0 \tag{4b}$$

where subscript i refers to either monomer (M) or dimer (D), D_L is the axial dispersion coefficient, u is the superficial velocity, L is the column length, and $\langle \hat{q}_i \rangle$ is the average protein concentration in the adsorbent particles. The expression used for the term $\partial \langle \hat{q}_i \rangle / \partial t$ in Eq. (4) depends on transport and kinetic resistances within the adsorbent particles. Once these intraparticle resistances are identified, extensions to account for non-uniform flow effects are easily implemented via, for example, computational fluid dynamics packages [27].

Our previous work [3] has shown that intraparticle transport of proteins in CHT occurs by a pore diffusion mechanism. The rates are lower for CHT Type I, which has smaller pores, than for CHT Type II, but the mechanism is qualitatively the same. Effective pore diffusivities, D_e, were determined previously from a van Deemeter analysis for non-binding conditions, and by CLSM for binding con-

Table 2
Rate parameters used in frontal analysis calculations. Effective pore diffusivities, D_e, are in 10^{-7} cm²/s. Rate constants for the Langmuir kinetics model, $k_{L,i}$, are in mL mg⁻¹ s⁻¹. Rate constants for the spreading kinetics model, $k_{S,i}$, are in s⁻¹.

CHT Type I		
	20 mM Na⁺	70 mM Na⁺
$D_{e,M}$	0.13*	0.58
$D_{e,D}$	0.08*	0.10
$k_{L,M}$	5.52	1.27
$k_{L,D}$	1.40	9.32
$K_{S,M}$	1.3	0.5
$K_{S,D}$	1.2	0.5
$k_{S,M}$	1.8×10^{-4}	1.2×10^{-4}
$k_{S,D}$	4.5×10^{-3}	1.8×10^{-3}

CHT Type II			
	20 mM Na⁺	70 mM Na⁺	100 mM Na⁺
$D_{e,M}$	1.1*	1.2	1.2
$D_{e,D}$	0.78*	0.78	0.78
$k_{L,M}$	0.03	0.05	0.02
$k_{L,D}$	1.30	0.10	0.17
$K_{S,M}$	2.7	0.2	0.1
$K_{S,D}$	11.3	4.5	2.9
$k_{S,M}$	1.5×10^{-4}	3.7×10^{-3}	1.8×10^{-5}
$k_{S,D}$	7.8×10^{-4}	1.3×10^{-3}	7.5×10^{-4}

* Data from ref. [3].

ditions for both single component and mixture adsorption. Similar D_e-values were obtained for binding and non-binding conditions for CHT Type II, but somewhat lower values of D_e were obtained under binding conditions for CHT Type I, likely because of the effects of the increased diffusional hindrance associated with bound proteins molecules in the smaller pores of this material. A summary of these parameters is given in Table 2. Accordingly, the term $\partial \langle \hat{q}_i \rangle / \partial t$ can be written as:

$$\frac{\partial \langle \hat{q}_i \rangle}{\partial t} = \frac{3D_{e,i}}{r_p} \frac{\partial c_i}{\partial r}\bigg|_{r=r_p} \tag{5}$$

where r_p is the particle radius and c_i is the protein concentration in the adsorbent particle pores. Note that these equations neglect the external boundary layer resistance since the Biot number ($Bi = k_f r_p / D_e$) is estimated to be in the range 40–100 based on established Sherwood number correlations for mass transfer in packed beds to estimate k_f [28].

4.1. Model for pore diffusion control

For conditions where the adsorption and displacement kinetics are completely controlled by intraparticle diffusion, adsorption equilibrium prevails at each point and time within the particles and is described by Eq. (1). Accordingly, the material balances for the particles are as follows:

$$\varepsilon_p' \frac{\partial c_M}{\partial t} + \frac{\partial q_M}{\partial t} = \frac{D_{e,M}}{r^2} \frac{\partial}{\partial r}\left(r^2 \frac{\partial c_M}{\partial r}\right) \tag{6a}$$

$$\varepsilon_p' \frac{\partial c_D}{\partial t} + \frac{\partial q_D}{\partial t} = \frac{D_{e,D}}{r^2} \frac{\partial}{\partial r}\left(r^2 \frac{\partial c_D}{\partial r}\right) \tag{6b}$$

$$r = 0, \frac{\partial c_M}{\partial r} = \frac{\partial c_D}{\partial r} = 0 \tag{6c}$$

$$r = r_p, c_M = C_M, c_D = C_D \tag{6d}$$

where

$$\frac{\partial q_M}{\partial t} = \frac{\partial q_M}{\partial c_M} \frac{\partial c_M}{\partial t} + \frac{\partial q_M}{\partial c_D} \frac{\partial c_D}{\partial t} \tag{7a}$$

$$\frac{\partial q_D}{\partial t} = \frac{\partial q_D}{\partial c_M}\frac{\partial c_M}{\partial t} + \frac{\partial q_D}{\partial c_D}\frac{\partial c_D}{\partial t} \tag{7b}$$

These partial derivatives are taken from the isotherm, Eq. (1).

4.2. Models incorporating adsorption kinetics resistances

As extensively reviewed, for example, by Rabe et al. [29], the kinetics of protein adsorption on solid surfaces is complex, potentially involving a variety of primary and secondary effects including structural rearrangements on the surface, cooperative adsorption, overshooting adsorption kinetics, and protein aggregation. The occurrence of protein conformational changes has been shown to occur both on ion exchange chromatography surfaces and on hydrophobic interaction chromatography media and has been found to be responsible for on-column aggregate formation [30,31], multiple peak elution [32], and irreversible binding [33]. In this work we did not observe aggregate formation or multiple peak elution, in part because of the lack of hydrophobicity on the CHT surface, which has been shown to play a major role on these effects. We also observed essentially stoichiometric recoveries of our antibody monomer and dimer samples upon elution from either CHT Type I or Type II using, for example, 500 mM phosphate as the eluent, either individually or in mixtures. Nevertheless, as demonstrated below, the experimental results exhibited displacement profiles that were considerably broader than those predicted assuming complete pore diffusion control. Moreover, as seen in Figs. 2 and 3, these profiles are asymmetrical suggesting that kinetic effects are at play in addition to diffusional transport limitation.

Lundstrom and Elwing [34] have provided a general framework for the description of these effects using simple kinetic expressions to model the exchange of protein molecules in solution for adsorbed molecules. Their key assumption is that the protein can exist in multiple bound states, which exchange with species in solution at different rates. The physical interpretation of these states varies and is often unknown, although the assumption is often made that the protein unfolds or spreads on the chromatographic surface resulting in strongly or irreversibly bound forms. This type of model, often referred to as "spreading kinetics", has been used previously by several authors to describe protein-surface interactions in different types of systems. For example, Yang and Etzel [35] modeled the kinetics of single component protein adsorption on an anion exchange membrane and found that spreading kinetics provided the best fit of asymmetrically skewed breakthrough curves. Because of the membrane format used, mass transfer effects were neglected. Haimer et al. [36] used a spreading model including an irreversibly bound state similar to that of Yang and Etzel to explain the two-peak elution behavior observed for certain proteins in hydrophobic interaction chromatography (HIC). Despite the relatively large size of the chromatographic particles used, these authors also neglected mass transfer effects, suggesting that the overall process was dominated by kinetics and unaffected by mass transfer. McCue et al. [37] developed a model including both mass transfer and spreading kinetics to describe the adsorption and elution of antibody monomer and aggregated species on an HIC resin. Their model was based on homogeneous diffusion with a driving force written in terms of the adsorbed phase protein concentration. Finally, Diedrich et al. [38] developed a multistate model combining spreading kinetics with the steric mass action (SMA) model to describe the adsorption of a mAb on ion exchange tentacle resins.

The kinetic model used in this work, also based on the Lundstrom and Elwing formalism, is illustrated in Fig. 4. With reference to this figure, we consider two bound states for each protein. The first bound state (shown by white circles and ovals for
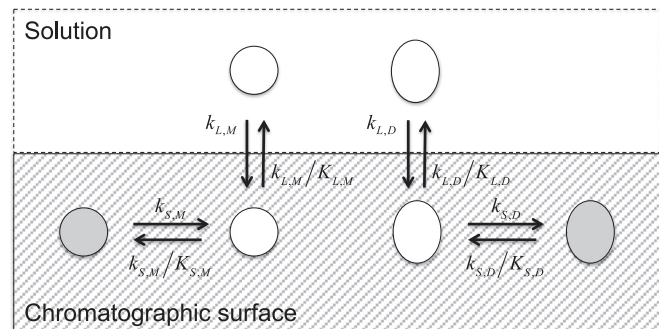

Fig. 4. Schematic representation of the spreading kinetics model for a two-component system. Circles and ovals represent monomer and dimer, respectively.

the monomer and dimer, respectively) is assumed to allow direct exchange with molecules in solution following a second order, competitive Langmuir kinetics. The second bound state (shown by gray circles and ovals for the monomer and dimer, respectively) is assumed to ensue from the first bound state following a reversible first order "spreading" kinetics. We assume that this new bound state is altered in a way that renders the bound molecules no longer amenable to direct exchange with molecules in solution. This mechanism is assumed to occur at each point within the particles and is considered along with diffusion in the particle pores. A key feature of this model is that, for conditions where adsorption is highly favorable, the spreading step does not affect the overall kinetics, which becomes dependent only on diffusion. On the other hand, the spreading kinetics included in this model affects both elution and frontal analysis since both molecules need to pass through the exchangeable bound state in order to desorb or undergo displacement. Intuitively, this mechanism can lead to the reversible, tailing displacement fronts observed during frontal analysis and, as will be shown later, tailing isocratic elution peaks.

The equations describing the kinetic scheme of Fig. 4 for a monomer/dimer mixture, including pore diffusion are as follows:

$$\varepsilon'_p \frac{\partial c_M}{\partial t} + r_{L,M} = \frac{D_{e,M}}{r^2}\frac{\partial}{\partial r}\left(r^2\frac{\partial c_M}{\partial r}\right) \tag{8a}$$

$$\varepsilon'_p \frac{\partial c_D}{\partial t} + r_{L,D} = \frac{D_{e,D}}{r^2}\frac{\partial}{\partial r}\left(r^2\frac{\partial c_D}{\partial r}\right) \tag{8b}$$

$$\frac{\partial q_{L,M}}{\partial t} = r_{L,M} - k_{S,M}\left(q_{L,M} - \frac{q_{S,M}}{K_{S,M}}\right) \tag{8c}$$

$$\frac{\partial q_{L,D}}{\partial t} = r_{L,D} - k_{S,D}\left(q_{L,D} - \frac{q_{S,D}}{K_{S,D}}\right) \tag{8d}$$

$$\frac{\partial q_{S,M}}{\partial t} = k_{S,M}\left(q_{L,M} - \frac{q_{S,M}}{K_{S,M}}\right) \tag{8e}$$

$$\frac{\partial q_{S,D}}{\partial t} = k_{S,D}\left(q_{L,D} - \frac{q_{S,D}}{K_{S,D}}\right) \tag{8f}$$

with:

$$r_{L,M} = k_{L,M}\left\{c_M\left[q_{m,M} - (q_{L,M} + q_{S,M}) - \frac{q_{m,M}}{q_{m,D}}(q_{L,D} + q_{S,D})\right] - \frac{q_{L,M}}{K_{L,M}}\right\} \tag{9a}$$

$$r_{L,D} = k_{L,D}\left\{c_D\left[q_{m,D} - (q_{L,D} + q_{S,D}) - \frac{q_{m,D}}{q_{m,M}}(q_{L,M} + q_{S,M})\right] - \frac{q_{L,D}}{K_{L,D}}\right\} \tag{9b}$$

In these equations, $q_{L,i}$ and $q_{S,i}$ represent the concentrations of protein that are, respectively, in the bound state that is directly exchangeable with molecules in solution and in the bound state that is not directly exchangeable; $r_{L,i}$ represents the rate of exchange with molecules in solution according to the Langmuir model,; and $k_{S,i}$ and $K_{S,i}$ are, respectively, the rate and equilibrium constants for the reversible conversion between the two bound states. Note that these equations assume that the two bound states occupy the same surface area, but this assumption can be relaxed with a minor modification of the model equations to describe other cases [34].

According to this model, adsorption equilibrium is described by the following equations:

$$q_{L,M} = \frac{q_{m,M}K_{L,M}C_M}{1 + K_{L,M}(1 + K_{S,M})C_M + K_{L,D}(1 + K_{S,D})C_D} \quad (10a)$$

$$q_{L,D} = \frac{q_{m,D}K_{L,D}C_D}{1 + K_{L,M}(1 + K_{S,M})C_M + K_{L,D}(1 + K_{S,D})C_D} \quad (10b)$$

$$q_M = q_{L,M} + q_{S,M} = \frac{q_{m,M}K_{L,M}(1 + K_{S,M})C_M}{1 + K_{L,M}(1 + K_{S,M})C_M + K_{L,D}(1 + K_{S,D})C_D} \quad (10c)$$

$$q_D = q_{L,D} + q_{S,D} = \frac{q_{m,D}K_{L,D}(1 + K_{S,D})C_D}{1 + K_{L,M}(1 + K_{S,M})C_M + K_{L,D}(1 + K_{S,D})C_D} \quad (10d)$$

where q_M and q_D are the total concentration of bound monomer and bound dimer, respectively, including both bound states.

Since the full model including both Langmuir kinetics and spreading kinetics would involve the simultaneous determination of many parameters, only two limiting cases are considered in this work, namely pore diffusion combined with Langmuir kinetics only, and pore diffusion combined with spreading kinetics only. The latter is obtained when $q_{L,M}$ and $q_{L,D}$ are in equilibrium with the local composition in the pore liquid, c_M and c_D. The model equations for the first of these two cases are obtained by setting $k_{S,i} = K_{S,i} = 0$ for $i = M$, D in Eqs. (8)–(9), while the model equations for the second case are as follows:

$$\varepsilon'_p \frac{\partial c_M}{\partial t} + \frac{\partial q_{L,M}}{\partial t} + r_{S,M} = \frac{D_{e,M}}{r^2}\frac{\partial}{\partial r}\left(r^2\frac{\partial c_M}{\partial r}\right) \quad (11a)$$

$$\varepsilon'_p \frac{\partial c_D}{\partial t} + \frac{\partial q_{L,D}}{\partial t} + r_{S,D} = \frac{D_{e,D}}{r^2}\frac{\partial}{\partial r}\left(r^2\frac{\partial c_D}{\partial r}\right) \quad (11b)$$

$$\frac{\partial q_{S,M}}{\partial t} = r_{S,M} \quad (11c)$$

$$\frac{\partial q_{S,D}}{\partial t} = r_{S,D} \quad (11d)$$

with

$$r_{S,M} = k_{S,M}\left(q_{L,M} - \frac{q_{S,M}}{K_{S,M}}\right) \quad (12a)$$

$$r_{S,D} = k_{S,D}\left(q_{L,D} - \frac{q_{S,D}}{K_{S,D}}\right) \quad (12b)$$

and

$$\frac{\partial q_{L,M}}{\partial t} = \frac{\partial q_{L,M}}{\partial c_M}\frac{\partial c_M}{\partial t} + \frac{\partial q_{L,M}}{\partial c_D}\frac{\partial c_D}{\partial t} \quad (13a)$$

$$\frac{\partial q_{L,D}}{\partial t} = \frac{\partial q_{L,D}}{\partial c_M}\frac{\partial c_M}{\partial t} + \frac{\partial q_{L,D}}{\partial c_D}\frac{\partial c_D}{\partial t} \quad (13b)$$

where the partial derivatives in Eqs. (13a) and (13b) are evaluated from Eq. (10a) and (10b).

Analytical solutions of these equations are only possible for the linear isotherm case. For the general case, a numerical solution was obtained for Eqs. (4)–(5) combined with: (a) Eqs. (6)–(7) for the case pore diffusion without kinetic resistance; (b) Eqs. (8)–(9) with

$k_{S,i} = K_{S,i} = 0$ with $i = M$, D for the case of pore diffusion combined with Langmuir kinetics; and (c) Eqs. (11)–(13) for the case of pore diffusion combined with spreading kinetics. In all three cases, the axial dispersion term was set to zero and the spatial derivative $\partial C_i/\partial x$ was approximated by Euler backwards finite differences method. This method introduces numerical dispersion, which was used to simulate axial dispersion by using a number of discretization points equal to the number of plates, $N = L/HETP$, determined from a pulse injection of the protein under non-binding conditions extrapolated to zero velocity according to the van Deemeter equation according to our previous data (Fig. 4 in ref. [3]). Radial derivatives were also discretized by finite differences resulting in a system of ordinary differential equations that, in turn, was solved using *ode15s* in MATLAB R2017b. (The Mathworks, Natick, MA, USA). The number of radial discretization points was set sufficiently large that increasing it further did not significantly affect the numerical results.

The model equations above are greatly simplified if the isotherms are assumed to be linear and non-competitive, with the following equations replacing Eqs. (10c) and (10d):

$$q_M = q_{m,M}K_{L,M}(1 + K_{S,M})C_M \quad (14a)$$

$$q_D = q_{m,D}K_{L,D}(1 + K_{S,D})C_D \quad (14b)$$

This result is approximated at relatively high Na^+ concentrations, when protein binding to the CHT surface is weak. Analytical solutions for this case are easily found in the Laplace domain and expressions for the moments of the isocratic elution peak are given in the Appendix. The corresponding first moment, HETP, and peak skew including pore diffusion and first order reversible spreading kinetics are found from the moments and are as follows:

$$\mu_1 = \frac{L}{v}\left(1 + k'\right) \quad (15)$$

$$H = \frac{2D_L}{v} + \frac{2v}{\phi}\left\{\left(\frac{k'}{1+k'}\right)^2\frac{r_p^2}{15D_e} + \left(\frac{\phi q_m K_L K_S}{1+k'}\right)^2\frac{1}{q_m K_L}\frac{1}{k_S}\right\} \quad (16)$$

Peak skew

$$= \frac{\frac{2L}{105v^5}\left\{\frac{2r_p^4 v^4 k'^3}{D_e^2\phi^2} + \frac{42r_p^2 v^2 k'\left[v^2 K_L K_S^2 q_m + D_e k_S k'\left(1+k'\right)/\phi\right]}{D_e k_S} + \frac{315\left[v^4\phi K_L K_S^3 q_m + 2v^2\phi D_e k_S K_L K_S^2 q_m\left(1+k'\right) + 2D_L^2 k_S^2\left(1+k'\right)^3\right]}{k_S^2}\right\}}{\left\{\frac{2Lr_p^2 k'^2}{15D_e v\phi} + \frac{2L}{k_S v^3}\left[v^2\phi K_L K_S^2 q_m + D_L k_S\left(1+k'\right)^2\right]\right\}^{\frac{3}{2}}} \quad (17)$$

where, for simplicity, the subscript i, identifying the component, has been dropped. In these expressions μ_1 is the first moment of the eluted peak, $\phi = (1 - \varepsilon)/\varepsilon$ is the phase ratio, and $k' = \phi[\varepsilon'_p + q_m K_L(1 + K_S)]$ is the retention factor. The limiting case of these equations for pore diffusion only is found by setting $k_S = \infty$ or $K_S = 0$.

5. Modeling results

5.1. Frontal analysis

Three different cases were considered to model the frontal analysis results – pore diffusion only without kinetic resistances, pore diffusion with Langmuir kinetics only, and pore diffusion with spreading kinetics only. For the first of these three cases, the calculations were done initially without adjusting any parameters using the experimentally determined isotherm parameters and the effective pore diffusivities from our prior work [3] summarized in Tables 1 and 2. For the other two cases, we used the same
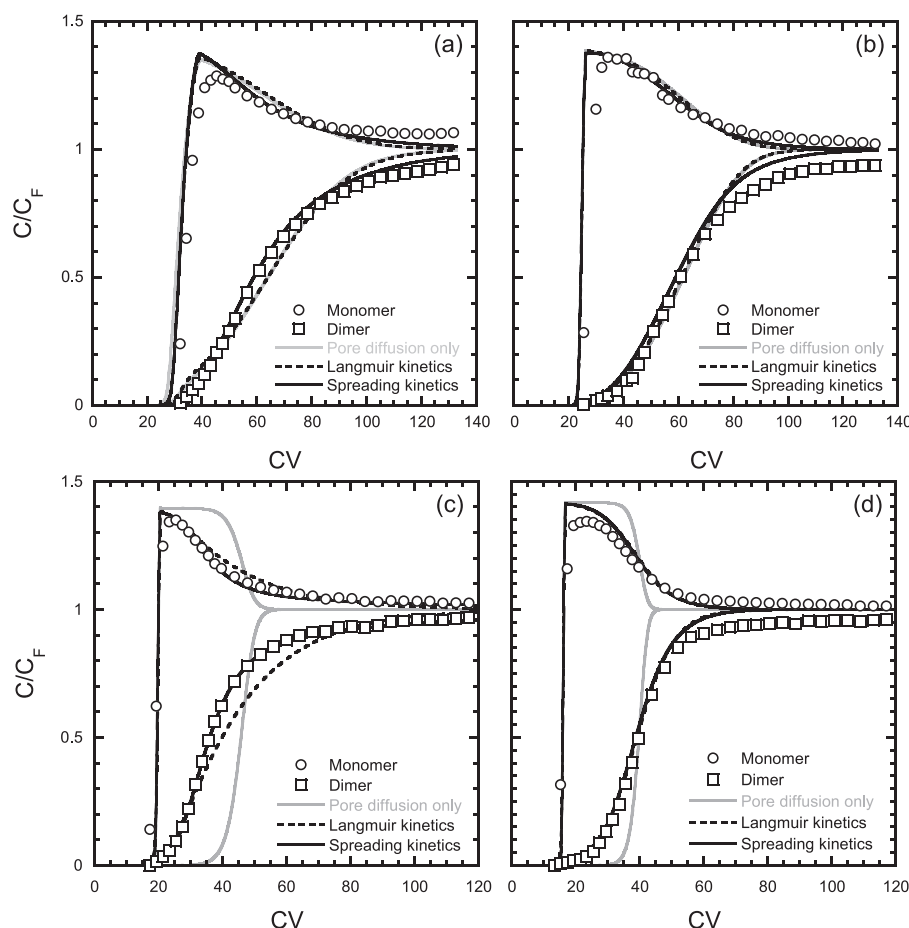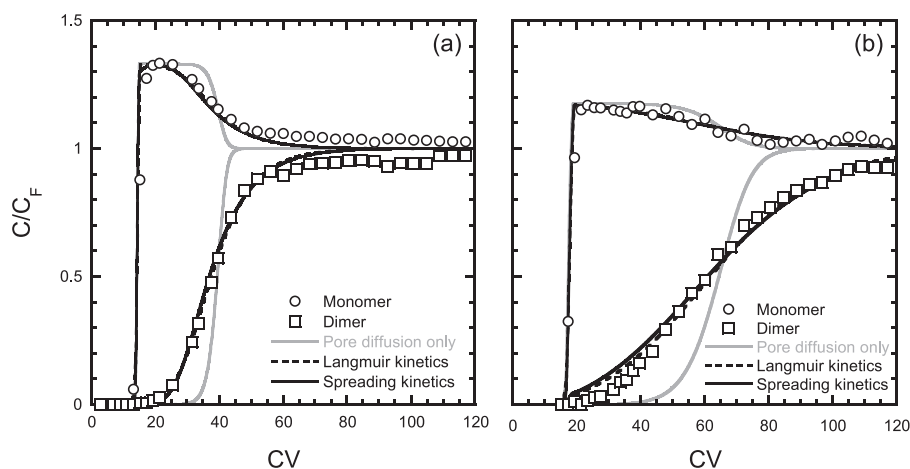
Fig. 5. Comparison of monomer-dimer binary breakthrough curves with calculations based on the pore diffusion model (solid gray lines), the pore diffusion model with Langmuir kinetics (dashed lines), and the pore diffusion model with spreading kinetics (solid black lines) using the two-component Langmuir isotherm (Eqs. (1)–(13)) to describe competitive binding. Experimental conditions are the same as in Fig. 2. The rate constants and effective diffusivities used in the numerical calculations are listed in Table 2.

isotherm and effective pore diffusivities as before but determined best-fit values of the rate parameters $k_{L,M}$ and $k_{L,D}$ for the Langmuir kinetics model and $K_{S,M}$, $K_{S,D}$, $k_{S,M}$ and $k_{S,D}$ for the spreading kinetics model at each Na$^+$ concentration. In each case, optimization of parameter values was done with the MATLAB nonlinear least squares function, *lsqnonlin*, which uses a steepest descent algorithm. Fitting the monomer/dimer displacement profiles only (instead of both pure monomer and monomer/dimer displacement fronts) proved easier to implement since the pure monomer front is very steep and even small horizontal deviations between experimental and predicted fronts resulted in unreasonable error estimates. A few test calculations considering both monomer and dimer profiles resulted in similar overall fits. Table 2 provides a summary of the parameters determined in this manner.

Fig. 5 compares the experimental results with calculates profiles based on the pore diffusion model without kinetic resistances, the pore diffusion combined with Langmuir kinetics, and the pore diffusion combined with spreading kinetics for CHT Type I and Type II at 20 and 70 mM Na$^+$. As seen in Fig. 5a and b, the experimental CHT Type I curves are very close to those predicted by the pore diffusion model without any kinetics resistance. This occurs because of the small pore size of this material which results in relatively small effective pore diffusivities and, thus, a dominance of mass transfer effects. Slightly better agreement is found in this case with either the fitted Langmuir kinetics model or the spreading kinetics model, but the difference between the two is minimal. On the other hand, as seen in Fig. 5c and d, the difference between

the CHT Type II experimental results and those predicted assuming pore diffusion only is quite large, especially at 20 mM Na$^+$. In this case, both kinetic models provide a description that is much closer to the experimental data. This is especially true for the spreading kinetics model that is able to describe the asymmetrically tailing displacement front observed at this low Na$^+$ concentration. For these conditions, the best-fit Langmuir kinetics model predicts a more monotonically curved displacement profile than is seen experimentally. On the other hand, the spreading kinetics model correctly describes the initially sharp displacement front followed by a long tail. The difference between the two kinetics models disappears, however, at the higher Na$^+$ concentration of 70 mM, which resulted in a steeper and more symmetrical displacement front. It should be noted that despite the added kinetics resistances, the CHT Type II curves are still, on the whole, considerably steeper than those observed for Type I because the diffusional resistance in the former material is smaller as a result of its larger pore size.

Fig. 6a shows experimental results for CHT Type II at 100 mM Na$^+$ along with model calculations using fitted rate parameters. For these conditions, the displacement front becomes much more symmetrical and even closer to the diffusion-controlled case making Langmuir and spreading kinetics models essentially indistinguishable from each other. Fig. 6b shows model predictions compared to experimental results at 70 mM Na$^+$ with a shorter residence time and a lower aggregate feed content using the rate parameters fitted to the data in Fig. 5d. These data are used as a test case to illustrate the ability of the model to predict the separation for

Fig. 6. Comparison of monomer-dimer binary breakthrough curves with predictions based on pore diffusion model (solid gray lines), the pore diffusion model with Langmuir kinetics mode (dashed lines), and the pore diffusion model with spreading kinetics model (solid black lines) using the two-component Langmuir isotherm (Eqs. (1)–(13)) to describe competitive binding of monomer and dimer. Experimental conditions are the same as in Fig. 3. The rate constants and effective diffusivities are listed in Table 2.

conditions outside those used to determine the model parameters. In this case, both Langmuir and spreading kinetics models, using the same parameters determined for the conditions of Fig. 5d, are able to predict quantitatively the experimental profiles. However, as shown below, only the spreading model can also simultaneous predict the intraparticle profiles and is, thus, more physically realistic. In this respect, we also attempted to describe the frontal analysis data with the pore diffusion model without kinetic resistances using the fitted effective diffusivities instead of the independently determined ones. In this case, as shown in the Supplementary Materials, although a good agreement could be found with the Type I results, where pore diffusion is actually dominant, only a rough agreement could be found for Type II especially at 20 mM Na^+ where the spreading effect is most significant. In this case, not only was the predicted shape of the displacement front inaccurate, but the D_e-values needed to fit the experimental profiles were 4 to 10 times smaller than those determined independently for the pure components (see Fig. S.3 in the Supplementary Materials).

The fitted kinetic rate parameters summarized in Table 2 show no particular trend relative to Na^+ concentration for the rate parameters $k_{L,M}$ and $k_{L,D}$ in the Langmuir kinetics model. On the other hand, the equilibrium constants $K_{S,M}$ and $K_{S,D}$ in the spreading kinetics model decrease steadily with Na^+ concentration suggesting that the tendency for the protein to spread on the CHT surface becomes less pronounced when binding becomes weaker. As indicated by the numerical values of these parameters, this effect appears to be especially pronounced for the dimer.

5.2. Intraparticle concentration profiles for batch adsorption

The goal of these experiments was to determine whether the same models used to fit the frontal analysis results is consistent with the intraparticle concentration profiles determined during batch co-adsorption by CLSM. As noted, for example, in ref. [39], for favorable adsorption isotherms, intraparticle concentration profiles are usually more sensitive to the nature of the assumed rate model compared to the breakthrough curves obtained from a column. This occurs because the batch measurements are not influenced by column dynamics or axial dispersion. Thus, they are essentially exclusively representative of equilibrium and rate effects.

In order to compare experimental and predicted profiles for these conditions, our previously obtained CLSM images for co-adsorption of monomer-dimer mixtures were digitized and converted to the individual monomer and dimer concentration profiles

at representative time points as described in ref. [18]. Since the experiments were done with a relatively low protein concentration (0.5 mg/mL each for monomer and dimer), the ensuing profiles reflect almost exclusively the bound protein concentration. Predicted profiles were obtained from the numerical solution of the same three models considered for the description of frontal analysis – pore diffusion only, pore diffusion with Langmuir kinetics, and pore diffusion with spreading kinetics – using the same equilibrium and rate parameters summarized in Tables 1 and 2. Fig. 7 shows the results for CHT Type I and Type II with a 20 mM Na^+ case, which gave the largest deviations between the different models in the frontal analysis experiments. As seen in this figure, the experimental CHT Type I concentration profiles are relatively sharp and in close agreement with those predicted by all three models. This result is expected because of the small effective diffusivity in this small pore material which results in a nearly completely diffusion controlled process. On the other hand, the CHT Type II profiles are comparatively smoother and deviate substantially from those predicted without accounting for any kinetic resistance. As seen in this figure, while the Langmuir kinetics model cannot predict the intraparticle behavior for these conditions, combining pore diffusion and spreading kinetics predicts profiles in good agreement with the experiments. Since the rate parameters used were the same that matched the frontal analysis data, this result supports the mechanistic validity of this model. Although the spreading model shows powerful predictive ability, a significant limitation of this modeling approach is that equilibrium adsorption data and at least some breakthrough experiments are required to calculate isotherm and spreading resistance as inputs for the model predictions.

5.3. Isocratic elution

This final set of experiments had two principal goals. The first was to help determine whether the kinetic resistance is exclusively associated with the monomer-dimer displacement or it can also affect the elution behavior of each individual species. The second goal was to determine if the same model that best describes the frontal analysis behavior could also be used to describe the isocratic elution behavior in the linear region of the isotherm attained at relatively high Na^+ concentrations. For these conditions the analytical solution of the equations describing the case of pore diffusion with spreading kinetics could be used directly to determine the model parameters by matching the experimental first
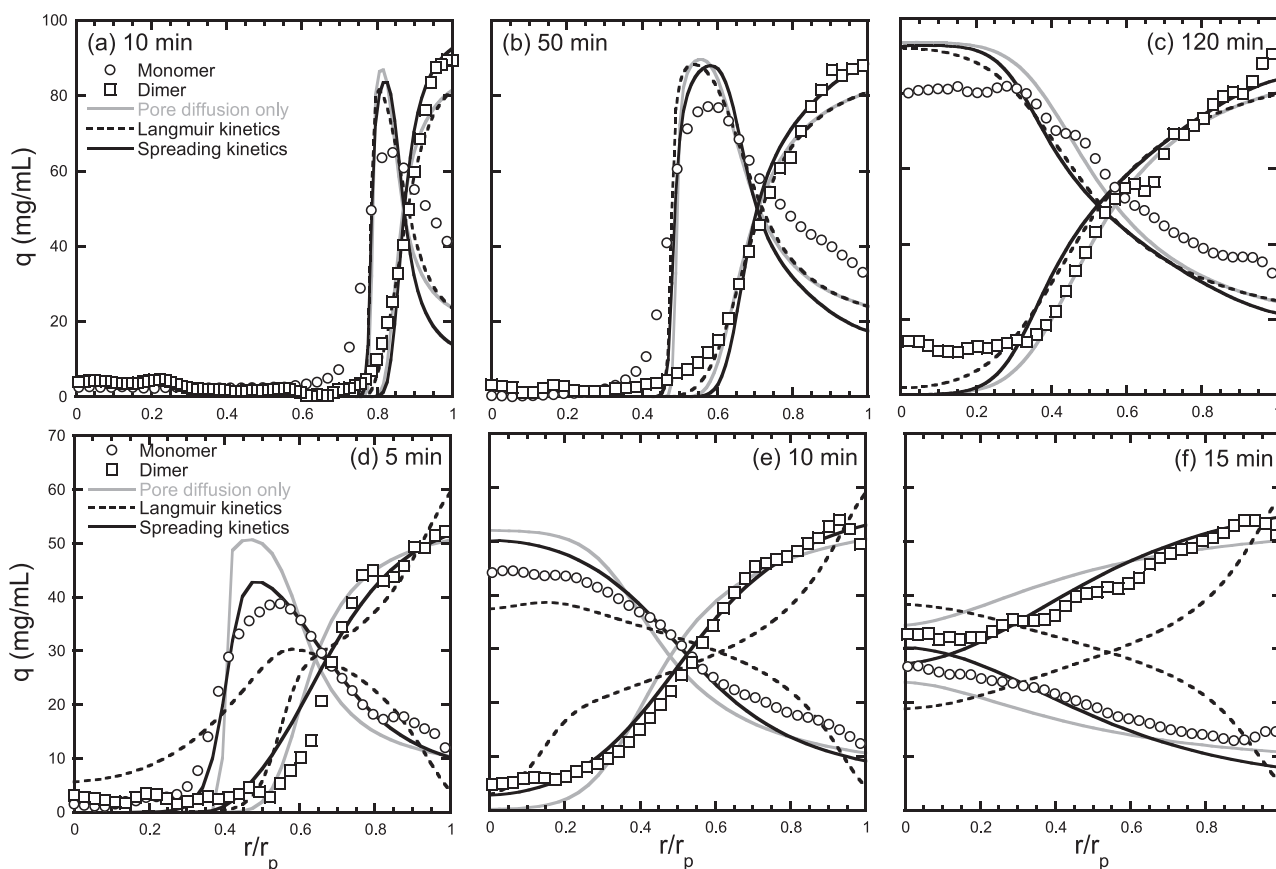
Fig. 7. Comparison of experimental and predicted intraparticle concentration profiles during co-adsorption of a 1 mg/mL monomer-dimer mixture containing 50% dimer in a 10 mM Na$_2$HPO$_4$ buffer at pH 7. Confocal microscopy images are from ref. [3]. Circles and squares are the normalized fluorescence intensity profiles of the monomer and dimer, respectively. Lines are model predictions based on the pore diffusion model (solid gray lines), the pore diffusion model with Langmuir kinetics (dashed lines), and the pore diffusion model with spreading kinetics (solid black lines) using the parameters listed in Table 2.

moment, the HETP, and the peak skew values with those predicted by Eqs. (15)–(17), independently for the monomer and for the dimer. Since the D_e-values are known, the model parameters for each component are $q_m K_L$, k_S, and K_S. In order to circumvent the difficulties encountered with the direct computation of moments, HETP and peak skew were obtained for each condition by fitting the exponentially modified Gaussian (EMG) function to the eluted peaks and using the expressions provided in ref. [40] to calculate the moments. An example is shown in the Supplementary Materials. $q_m K_L$, k_S, and K_S were then calculated based on Eqs. (15)–(17) using the known D_e-values.

Fig. 8 compares the isocratic elution model and data. The corresponding first moment, HETP, and peak skew values are given in Table 3 along with the model parameters based on the experimental values. Linear isotherm conditions were checked by injecting different amounts of protein and verifying that there was no effect on the peak shape (results not shown for brevity). As seen in Fig. 8a and in Table 3, the HETP increases only slightly when the Na$^+$ concentration is decreased for the monomer on CHT Type I. In this case, the experimental peaks are in very close agreement with predictions based on pore diffusion only suggesting that kinetics effects are insignificant. A larger contribution of kinetic effects can be seen for the dimer on CHT Type I (Fig. 8b), for the monomer of CHT Type II (Fig. 8c), and, especially, for the dimer on CHT Type II (Fig. 8d). These effects become more important as the Na$^+$ concentration is reduced and the binding strength increases. As seen in Fig. 8d for the dimer on CHT Type II, the elution peak becomes highly asymmetrical and very broad compared to predictions based on pore diffusion alone. The values of parame-

ters of the spreading kinetics model (including pore diffusion) provide some useful clues. Retention, of course, increases at the Na$^+$ concentration is reduced, which is reflected in the increasing values of $q_m K_L$. However, K_S also increases substantially as the Na$^+$ concentration is reduced and binding becomes stronger. In agreement with the results obtained by fitting the full model to the frontal analysis data, this result suggests again that the tendency to spread on the CHT surface increases as binding becomes stronger especially for the dimer. k_S remains, however, relatively constant with Na$^+$ concentration, indicating that the equilibrium distribution of the different bound states is the principal driver of the experimentally observed peak skewness at low Na$^+$ concentrations. As seen in Fig. 8, peak shapes calculated using the parameters in Table 3 and the numerical solution of the model equations are in good agreement with the experimental peaks, further corroborating the validity of the model.

6. Conclusions

The separation of antibody monomer-dimer mixtures by frontal analysis was obtained using either CHT Type I or Type II columns at residence times between 2.5 and 5.6 min indicating that the adsorption dynamics are sufficiently fast in both cases to attain practical separations. The two component breakthrough curves consist of a pure monomer front followed by a monomer-dimer displacement front. Relatively pure monomer, which is the more weakly bound species, is recovered between the two fronts. The binding capacities obtained from the frontal analysis data agree with Langmuir model predictions over a range of Na$^+$ concentrations in the
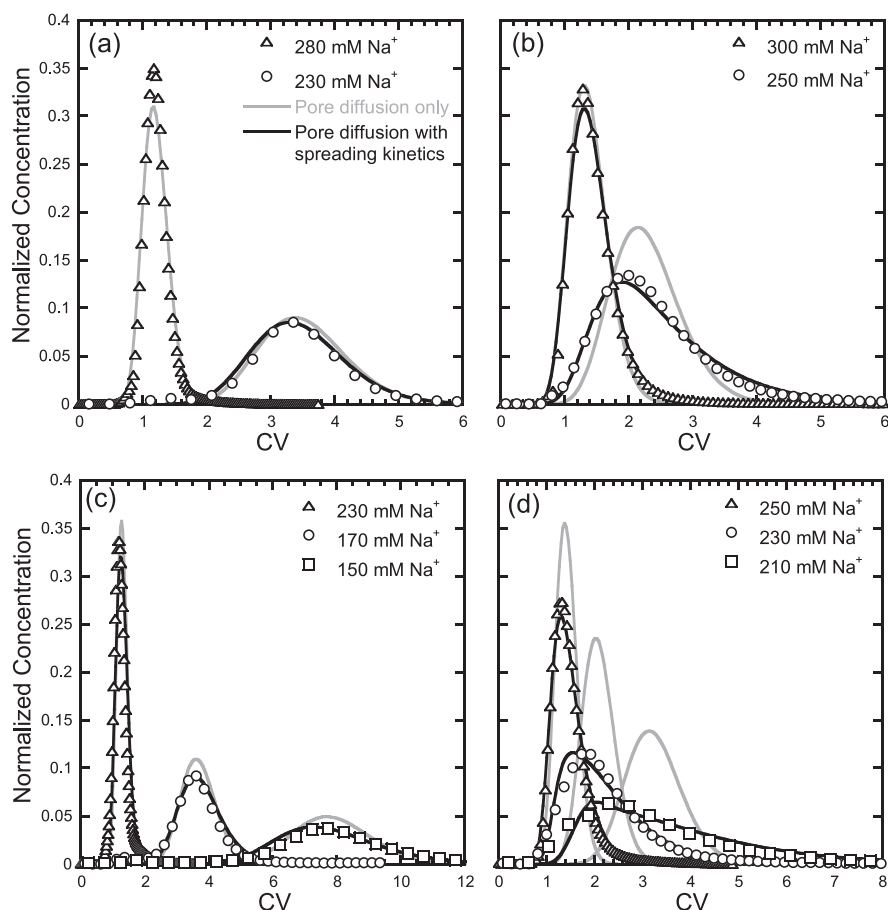
Fig. 8. Isocratic elution profiles on CHT Type I (a, b) and CHT Type II (c, d) for the mAb monomer (a, c) and dimer (b, d) obtained at different Na+ concentrations in sodium phosphate buffers containing different Na+ concentrations at pH 7.

Table 3

Parameters for pore diffusion plus spreading kinetics model based on the moments of the isocratic elution peaks. Parameters were derived based on effective pore diffusivities 5.4×10^{-8} and 9.4×10^{-8} cm^2/s for the monomer in CHT Type I and Type II, respectively, and 3.3×10^{-8} and 6.6×10^{-8} cm^2/s for the dimer in CHT Type I and Type II, respectively, and an axial dispersion coefficient based on $2D_L/v$=0.037 cm according to ref. [3].

CHT Type I							
	Na+ (mM)	Exp. μ_1(s)	Exp. HETP (cm)	Exp. Peak skew	$q_m K_L$	k_S (s^{-1})	K_S
Monomer	280	480	0.16	0.39	0.77	ND*	ND*
	230	1410	0.34	0.79	3.99	5.4×10^{-5}	0.015
Dimer	300	550	0.52	1.26	1.00	6.3×10^{-4}	0.076
	250	920	1.17	1.32	1.59	3.0×10^{-3}	0.49

CHT Type II							
	Na+ (mM)	Exp. μ_1 (s)	Exp. HETP (cm)	Exp. Peak skew	$q_m K_L$	k_S (s^{-1})	K_S
Monomer	230	520	0.17	0.79	0.79	6.3×10^{-4}	0.039
	170	1470	0.27	0.78	3.88	6.8×10^{-4}	0.083
	150	3200	0.35	0.80	9.02	5.7×10^{-4}	0.15
Dimer	250	580	0.48	1.23	0.77	5.2×10^{-3}	0.37
	230	850	1.38	1.40	0.93	7.1×10^{-3}	1.16
	210	1320	1.98	1.43	1.57	4.4×10^{-3}	1.32

* Experimental HETP was consistent with pore diffusion only.

load buffer. However, kinetic effects are pronounced resulting in separations that are not as good as predicted under ideal conditions. For CHT Type I, which has smaller pores, adsorption is nearly completely dominated by pore diffusion. Conversely, for CHT Type II, which has larger pores, columns dynamics results from a combination of pore diffusion and binding kinetics, the latter becomes more pronounced as the salt concentration is reduced and protein binding becomes stronger. Although sharper breakthrough fronts are obtained at higher salt concentrations because of the reduced

impact of adsorption kinetics, the binding capacity decreases leading to a smaller distance between the pure monomer front and the monomer-dimer displacement front requiring a trade-off of capacity and rates.

Three different column dynamic models based on different mechanistic assumptions were tested for their ability to describe the experimental results and predict separations – a pore diffusion model, a pore diffusion model with Langmuir adsorption kinetics, and a pore diffusion model with spreading kinetics

where adsorbed molecules are hypothesized to exist in two different interconvertible bound states, one freely exchangeable for molecules in solution and the other not at all directly exchangeable with molecules in solution. The spreading model provided the best description of the CHT Type II frontal analysis data and could be used to predict the effects of feed concentration, percentage of dimer in the feed, and residence time. This model could also predict the intraparticle concentration profiles observed by confocal microscopy during co-adsorption of monomer-dimer mixtures on individual CHT particles. Finally, the spreading kinetic model was corroborated by comparing experimental results and model predictions for isocratic elution for conditions where the isotherm is linear using rate parameters determined from the moments of the experimental peaks. These results show that the spreading kinetics model, including pore diffusion, can also describe the low-loading isocratic elution behavior with parameters that follow trends similar to those observed for the frontal analysis case, suggesting that the postulated existence of multiple binding sites is likely responsible not only for the displacement kinetics but also the elution behavior of each individual monomer and dimer species. A final consideration is a comparison of the two different CHT types used in this work. Since the hydroxyapatite crystals are chemically the same in both Type I and Type II, the main difference is the pore size, which is considerably smaller in Type I. The net result is that while the binding capacity of Type I is higher, intraparticle diffusion of mAb monomer and dimer is much slower than for Type II. As a result of pronounced mass transfer effect in Type I, spreading on the surface is less important. However, the overall rate of Type I is still slower than Type II. From the practical viewpoint, whether Type I or Type II is chosen will, thus, depend on whether capacity or process speed are more important, with the former being better for Type I and the latter for Type II.

Declaration of Competing Interest

The authors declare that they have no known competing financial interests or personal relationships that could have appeared to influence the work reported in this paper.

Acknowledgements

Supplementary materials

Supplementary material associated with this article can be found, in the online version, at doi:10.1016/j.chroma.2019.460504.

Appendix

For the linear isotherm case, analytical solution can be obtained easily in the Laplace domain. The moments of the pulse response peak can then be derived explicitly using the van der Laan theorem as shown, for example, in refs. [41–43]. Column dynamics including pore diffusion combined with spreading kinetics is described by the following equations and boundary conditions:

$$\varepsilon D_L \frac{\partial^2 C}{\partial x^2} = u \frac{\partial C}{\partial x} + \varepsilon \frac{\partial C}{\partial t} + (1-\varepsilon) \frac{3 D_e}{r_p} \frac{\partial c}{\partial r}\bigg|_{r=r_p} \tag{A1}$$

$$x = 0, C = C^F \tag{A1a}$$

$$x = L, \frac{\partial C}{\partial x} = 0 \tag{A1b}$$

$$\left(\varepsilon'_p + q_m K_L\right) \frac{\partial c}{\partial t} + r_S = \frac{D_e}{r^2} \frac{\partial}{\partial r}\left(r^2 \frac{\partial c}{\partial r}\right) \tag{A2}$$

$$r = 0, \frac{\partial c}{\partial r} = 0 \tag{A2a}$$

$$r = r_p, c = C \tag{A2b}$$

$$r_S = k_S\left(q_m K_L c - \frac{q_S}{K_S}\right) \tag{A3}$$

$$\frac{\partial q_S}{\partial t} = r_S \tag{A4}$$

where, for simplicity, subscript i, identifying the component, has been dropped. In the Laplace domain, these equations become:

$$\frac{d^2 \tilde{C}}{dx^2} - \frac{v}{D_L}\frac{d\tilde{C}}{dx} - \frac{s}{D_L}\tilde{C} - \frac{3\phi D_e}{D_L r_p}\frac{d\tilde{c}}{dr}\bigg|_{r=r_p} = 0 \tag{A5}$$

$$\left(\varepsilon'_p + q_m K_L\right)s\tilde{c} + k_S q_m K_L\left(\tilde{c} - \frac{\tilde{q}_S}{q_m K_L K_S}\right) = \frac{D_e}{r^2}\frac{d}{dr}\left(r^2\frac{d\tilde{c}}{dr}\right) \tag{A6}$$

$$s\tilde{q}_S = k_S q_m K_L\left(\tilde{c} - \frac{\tilde{q}_S}{q_m K_L K_S}\right) \tag{A7}$$

Combining Eqs. (A6) and (A7) yields:

$$\frac{1}{r^2}\frac{d}{dr}\left(r^2\frac{d\tilde{c}}{dr}\right) = a\tilde{c} \tag{A8}$$

where

$$a = \frac{\left(\varepsilon'_p + q_m K_L\right)s}{D_e} + \frac{q_m K_L K_S}{D_e}\frac{s}{1 + sK_S/k_S} \tag{A9}$$

Solution of this ODE subject to boundary conditions A2a and A2b gives:

$$\tilde{c} = \tilde{C}\frac{exp\left[(r_p - r)\sqrt{a}\right]\left(-1 + e^{2r\sqrt{a}}\right)}{\left(-1 + e^{2r_p\sqrt{a}}\right)r/r_p} \tag{A10}$$

$$\frac{d\tilde{c}}{dr}\bigg|_{r=r_p} = \tilde{C}\left[-\sqrt{a} - \frac{1}{r_p} + \frac{2\sqrt{a}e^{2r_p\sqrt{a}}}{-1 + e^{2r_p\sqrt{a}}}\right] \tag{A11}$$

Finally, combining this equation with Eq. (A5) and integrating with boundary conditions A1a and A1b gives the following result for the column transfer function:

$$\frac{\tilde{C}}{\tilde{C}^F}$$
$$= exp\left\{\frac{vL}{2D_L} - \frac{vL}{2D_L}\sqrt{1 + \frac{4D_L}{v^2}\left[s + \frac{3\phi D_e}{r_p}\left(-\sqrt{a} - \frac{1}{r_p} + \frac{2\sqrt{a}e^{2r_p\sqrt{a}}}{-1 + e^{2r_p\sqrt{a}}}\right)\right]}\right\} \tag{A12}$$
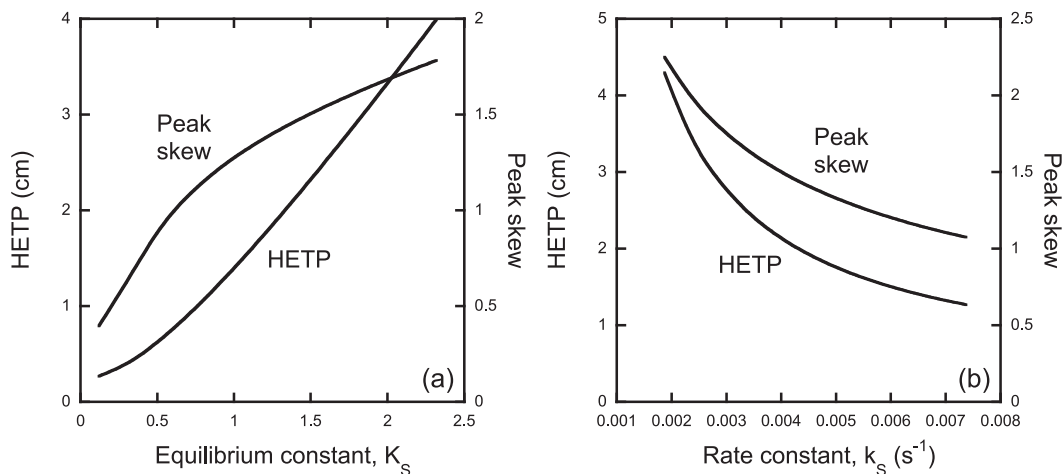
The central moments of the pulse response peak are found from the following equations:

$$\mu_0 = \lim_{s\to 0}\tilde{C}(s, L) \tag{A13}$$

$$\mu_1 = -\frac{1}{\mu_0}\lim_{s\to 0}\frac{d\tilde{C}(s, L)}{ds} \tag{A14}$$

$$\mu'_2 = \frac{1}{\mu_0}\lim_{s\to 0}\frac{d^2\tilde{C}(s, L)}{ds^2} - (\mu_1)^2 \tag{A15}$$

$$\mu'_3 = -\frac{1}{\mu_0}\lim_{s\to 0}\left[\frac{d^3\tilde{C}(s, L)}{ds^3}\right] - 3\mu_1\mu_2 + 2(\mu_1)^2 \tag{A16}$$

Fig. A1. Theoretical effects of the equilibrium constant, K_S, and of the rate constant, k_S, in the pore diffusion model with spreading kinetics on HETP and peak skew. Calculations are shown as an example for the dimer on CHT Type II at 210 mM Na$^+$ for the conditions of Table 3. The retention factor was kept constant in these calculations.

which yield:

$$\mu_1 = \frac{L}{v}\left(1 + k'\right) \tag{A17}$$

$$\mu'_2 = \frac{2Lr_p^2 k'^2}{15 D_e v\phi} + \frac{2L}{k_S v^3}\left[v^2 \phi q_m K_L K_S^2 + D_L k_S \left(1 + k'\right)^2\right] \tag{A18}$$

$$\mu'_3 = \frac{2L}{105 v^5}\left\{\frac{2r_p^4 v^4 k'^3}{D_e^2 \phi^2} + \frac{42 r_p^2 v^2 k'\left[v^2 q_m K_L K_S^2 + D_L k_S k'\left(1+k'\right)/\phi\right]}{D_e k_S}\right.$$
$$\left. + \frac{315\left[v^4 \phi q_m K_L K_S^3 + 2v^2 \phi D_L q_m K_L k_S K_S^2\left(1+k'_i\right) + 2D_L^2 k_S^2 (1+k')^3\right]}{k_S^2}\right\} \tag{A19}$$

where $k' = \phi[\varepsilon_p + q_m K_L(1 + K_S)]$ is the retention factor. These expressions were obtained using Wolfram Mathematica® 10. HETP and peak skew were then calculated as:

$$H = \frac{\mu'_2 L}{(\mu_1)^2} \tag{A20}$$

$$\text{Peakskew} = \frac{\mu'_3}{(\mu'_2)^{3/2}} \tag{A21}$$

Fig. A1 shows the theoretical effects of the equilibrium constant, K_S, and of the rate constant, k_S, on HETP and peak skew for the dimer on CHT Type II at 210 mM Na$^+$ for the conditions of Table 3. As seem from this figure, increasing K_S, which corresponds to greater tendency to spread, increases both HETP and peak skew, while increasing k_S, which corresponds to faster spreading kinetics, reduces both.

References

[1] D. Malina, K. Biernat, A. Sobczak-kupiec, Studies on sintering process of synthetic hydroxyapatite, Acta Biochim. Pol. 60 (2013) 851–855.
[2] C.F. Ramirez-Gutierrez, S.M. Londoño-Restrepo, A. Real, M.A. Mondragón, Effect of the temperature and sintering time on the thermal, structural, morphological, and vibrational properties of hydroxyapatite derived from pig bone, Ceram. Int. 43 (2017) 7552–7559.
[3] Y. Wang, G. Carta, Competitive binding of monoclonal antibody monomer-dimer mixtures on ceramic hydroxyapatite, J. Chromatogr. A 1587 (2019) 136–145.
[4] M.J. Gorbunoff, The interaction of proteins with hydroxyapatite: I. Role of protein charge and structure, Anal. Biochem. 136 (1984) 425–432.
[5] M.J. Gorbunoff, The interaction of proteins with hydroxyapatite: II. Role of acidic and basic groups, Anal. Biochem. 136 (1984) 433–439.
[6] M.J. Gorbunoff, S.N. Timasheff, The interaction of proteins with hydroxyapatite: III. Mechanism, Anal. Biochem. 136 (1984) 440–445.
[7] L.J. Cummings, M.A. Snyder, K. Brisack, Protein chromatography on hydroxyapatite columns, chapter 24, Meth. Enzymol. 463 (2009) 387–404.
[8] R. Giovannini, R. Freitag, Comparison of different types of ceramic hydroxyapatite for the chromatographic separation of plasmid DNA and a recombinant anti-Rhesus d antibody, Biosep 9 (2000) 359–368.
[9] E. Schmoeger, C. Paril, R. Tscheliessnig, A. Jungbauer, Adsorption of plasmid dna on ceramic hydroxyapatite chromatographic materials, J. Sep. Sci. 33 (2010) 3125–3136.
[10] X.L. Shi, M.Q. Feng, J. Shi, Z.H. Shi, J. Zhong, P. Zhou, High-level expression and purification of recombinant human catalase in pichia pastoris, Prot. Expr. Purif. 54 (2007) 24–29.
[11] J.C. Cook, J.G. Joyce, H.A. George, L.D. Schultz, W.M. Hurni, K.U. Jansen, R.W. Hepler, C. Ip, R.S. Lowe, P.M. Keller, E.D. Lehman, Purification of virus-like particles of recombinant human papillomavirus type 11 major capsid protein L1 from saccharomyces cerevisiae, Prot. Expr. Purif. 17 (1999) 477–484.
[12] A. Jungbauer, R. Hahn, K. Deinhofer, P. Luo, Performance and characterization of a nanophased porous hydroxyapatite for protein chromatography, Biotechnol. Bioeng. 87 (2004) 364–375.
[13] M. Saito, Y. Kurosawa, T. Okuyama, Purification of anti-japanese encephalitis virus monoclonal antibody by ceramic hydroxyapatite chromatography without proteins a and g, Hybridoma 31 (2012) 68–71.
[14] P. Gagnon, Improved antibody aggregate removal by hydroxyapatite chromatography in the presence of polyethylene glycol, J. Immunol. Methods. 336 (2008) 222–228.
[15] S. Sun, C. Gallo, B. Kelley, Removal of High Molecular Weight Aggregates using Hydroxyapatite Chromatography, US Patent 9,469,672, 2016.
[16] M. Vázquez-Rey, D.A. Lang, Aggregates in monoclonal antibody manufacturing processes, Biotechnol. Bioeng. 108 (2011) 1494–1508.
[17] Y. Tao, N. Chen, G. Carta, G. Ferreira, D. Robbins, Modeling multicomponent adsorption of monoclonal antibody charge variants in cation exchange columns, AIChE J. 58 (2012) 2503–2511.
[18] J.M. Reck, T.M. Pabst, A.K. Hunter, G. Carta, Separation of antibody monomer-dimer mixtures by frontal analysis, J. Chromatogr. A 1500 (2017) 96–104.
[19] A.K. Hunter, G. Carta, Effects of bovine serum albumin heterogeneity on frontal analysis with anion-exchange media, J. Chromatogr. A 937 (2001) 13–19.
[20] W.F. Weinbrennef, M.R. Etzel, Competitive adsorption of α-lactalbumin and bovine serum albumin to a sulfopropyl ion-exchange membrane, J. Chromatogr. A 662 (1994) 414–419.
[21] H.F. Liu, B. Mccooey, T. Duarte, D.E. Myers, T. Hudson, A. Amanullah, R. Van Reis, B.D. Kelley, Exploration of overloaded cation exchange chromatography for monoclonal antibody purification, J. Chromatogr. A 1218 (2011) 6943–6952.
[22] M.T. Stone, K.A. Cotoni, L. Jayson, Cation exchange frontal chromatography for the removal of monoclonal antibody aggregates, J. Chromatogr. A (2019).
[23] B.R.B. Wollacott, L.E. Roth, T.L. Sears, R.A. Sharpe, M. Jiang, S.S. Ozturk, The development of a flow-through mode cation exchange process for the purification of a monoclonal antibody, Bioproc. J. 14 (2015).
[24] J.M. Reck, T.M. Pabst, A.K. Hunter, X. Wang, G. Carta, Adsorption equilibrium and kinetics of monomer – dimer monoclonal antibody mixtures on a cation exchange resin, J. Chromatogr. A 1402 (2015) 46–59.
[25] D.M. Ruthven, Principles of Adsorption and Adsorption Processes, John Wiley & Sons, 1984.
[26] G. Carta, A. Jungbauer, Protein Chromatography - Process Development and Scale-Up, John Wiley & Sons, 2010.
[27] P. Gzil, G.V. B.aron, G. Desmet, Computational fluid dynamics simulations yielding guidelines for the ideal internal structure of monolithic liquid chromatography, J. Chromatogr. A 991 (2003) 169–188.
[28] E.J. Wilson, C.J. Geankoplis, Liquid mass transfer at ever low Reynolds numbers in packed beds, Ind. Eng. Chem. Fundam. 5 (1966) 9–14.

[29] M. Rabe, D. Verdes, S. Seeger, Understanding protein adsorption phenomena at solid surfaces, Adv. Coll. Int. Sci. 162 (2011) 87–106.

[30] J. Guo, S. Zhang, G. Carta, Unfolding and aggregation of a glycosylated monoclonal antibody on a cation exchange column. Part I. Chromatographic elution and batch adsorption behavior, J. Chromatogr. A 1356 (2014) 117–128.

[31] J. Guo, G. Carta, Unfolding and aggregation of a glycosylated monoclonal antibody on a cation exchange column. Part II. Protein structure effects by hydrogen deuterium exchange mass spectrometry, J. Chromatogr. A 1356 (2014) 129–137.

[32] J. Guo, A.D. Creasy, G. Barker, G. Carta, Surface induced three-peak elution behavior of a monoclonal antibody during cation exchange chromatography, J. Chromatogr. A 1474 (2016) 85–94.

[33] A. Jungbauer, C. Machold, R. Hahn, Hydrophobic interaction chromatography of proteins: III. Unfolding of proteins upon adsorption, J. Chromatogr. A 1079 (2005) 221–228.

[34] I. Lundström, H. Elwing, Simple kinetic models for protein exchange reactions on solid surfaces, J. Coll. Int. Sci. 136 (1990) 68–84.

[35] H. Yang, M.R. Etzel, Evaluation of three kinetic equations in models of protein purification using ion-exchange membranes, Ind. Eng. Chem. Res. 42 (2003) 890–896.

[36] E. Haimer, A. Tscheliessnig, R. Hahn, A. Jungbauer, Hydrophobic interaction chromatography of proteins iv kinetics of protein spreading, J. Chromatogr. A 1139 (2007) 84–94.

[37] J.T. McCue, P. Engel, A. Ng, R. Macniven, J. Thommes, Modeling of protein monomer/aggregate purification and separation using hydrophobic interaction chromatography, Biopr. Biosyst. Eng. 31 (2008) 261–275.

[38] J. Diedrich, W. Heymann, S. Leweke, S. Hunt, R. Todd, C. Kunert, W. Johnson, E. von Lieres, Multi-state steric mass action model and case study on complex high loading behavior of mAb on ion exchange tentacle resin, J. Chromatogr. A 1525 (2017) 60–70.

[39] G. Carta, A.R. Ubiera, T.M. Pabst, Protein mass transfer kinetics in ion exchange media: measurements and interpretations, Chem. Eng. Technol. 28 (2005) 1252–1264.

[40] E. Grushka, Characterization of exponentially modified peaks in chromatography, Anal. Chem. 44 (1972) 1733–1738.

[41] P. Schneider, J.M. Smith, Adsorption rate constants from chromatography, AIChE J. 14 (1968) 762-tt1.

[42] S. Qamar, J.N. Abbasi, S. Javeed, A. Seidel-Morgenstern, Analytical solutions and moment analysis of general rate model for linear liquid chromatography, Chem. Eng. Sci. 107 (2014) 192–205.

[43] S. Qamar, N. Akram, A. Seidel-Morgenstern, Analysis of general rate model of linear liquid chromatography considering finite rates of the adsorption and desorption steps, Chem. Eng. Res. Des. 111 (2016) 13–23.